Study on Mechanical Properties and Failure Mechanism of Medium Manganese TRIP Steel / DP590 Dissimilar Steel Resistance Spot Welding Joint

Hongning Liu[a,b] (ID)*, Yunming Zhu[a,b]* (ID)*, Yifeng Tian[a,b], Fufa Wei[a,b], Yongqiang Zhou[a,b],*

Zhengqiang Zhu[a,b]* (ID)

[a]*Nanchang University, College of Advanced Manufacturing, Nanchang, China.*
[b]*Jiangxi Provincial Key Laboratory of Robot and Welding Automation, Nanchang, China.*

This paper presents the resistance spot welding process test and numerical simulation analysis of medium manganese steel TRIP steel (7MnSteel) and DP590 steel plate. The results show that the failure mode is PF-TT failure, and IF and PF-TT are investigated. At the same time, based on the numerical simulation under the typical welding parameters, the welding plate has the stress concentration at the electrode edge at the beginning of the welding. Along with the welding, there is the stress concentration in the heat-affected zone of the medium manganese TRIP steel, which may also be the reason for the failure of the joint here. The current density is concentrated at the contact surface between the electrode and the weld plate, and the error in the diameter of the nugget measured by simulation and experiment is within 7%, which verifies the accuracy and reliability of the model.

Keywords: *Resistance spot welding; medium manganese TRIP steel; DP590; numerical simulation; failure mode.*

1. Introduction

Research information from the World Aluminium Association shows that for every 1% reduction in the overall vehicle mass, fuel efficiency can be improved by 0.6%-0.8% and CO_2 emissions can be reduced by 0.45%; for a 100 kg reduction in the overall vehicle mass, the fuel consumption of the vehicle can be reduced by 0.3-0.6 liters per 100 km[1]. Medium-manganese TRIP steel as the third generation of high-strength steel has received much attention due to its excellent mechanical properties[2-4]. The medium manganese TRIP steel matrix generally consists of residual austenite with face-centered cubic structure and ferrite with body-centered cubic structure[5-7]. The 37% residual austenite in the ferrite matrix leads to an ultimate tensile strength of 1193 MPa and an excellent elongation of >25%[8]. Usually a car is spliced by 3000-5000 welding joints, and resistance spot welding has become one of the main connection technologies in automotive manufacturing due to its high productivity, low cost, easy welding quality assurance and easy automation, with high current, short time, low workpiece deformation and stress. Therefore, good resistance spot welding performance is the key to the study of medium manganese TRIP steel[9-12].

Jia et al.[13] of Tsinghua University studied the resistive point welding process of cold rolled 0.1C-5Mn with ferric matrix and Sub-stable austenitic biphasic organization. The nugget size increased with increasing welding heat input, but the tensile shear load increased slowly when the welding current exceeded a critical value, and two different failure modes, IF and PIF, were observed. Park et al.[14] compared the Microstructure, tensile properties and fracture behavior

between resistance spot welding of medium manganese TRIP steel and resistance spot welding of medium manganese steel and DP980 dissimilar steel. It was found that using pre-pulse current to increase the width of nugget size is unnecessary to improve weldability. Li et al.[15] studied the welding properties of three resistance spot welding devices for medium manganese steel in Fe-7Mn-0.14C, and found that adding gasket 3D welding device can significantly improve the overall mechanical properties of resistance spot welding of medium manganese steel.

The invisibility of the resistance spot welding nugget formation and the transient nature of the welding process greatly increase the difficulty of experimental studies and observations, while the numerical simulation of the spot welding process is not limited by the actual welding conditions. The finite element model not only saves cost, but also easily changes parameters to optimize experimental parameter design[16-18]. Since the initial finite element spot welding analysis model established by Nied[19] in 1984, many finite element models of spot welding have appeared, and provide a theoretical basis for practical production[20-23]. Raoelison et al.[24], University of Brittany, France, studied how to improve the calculation accuracy of resistance spot welding of advanced galvanized steel sheets with circular tip electrodes. Experimental analysis was performed to highlight the considerations required for the numerical simulations. Lu et al.[25] of Ohio State University established a three-dimensional fully coupled electric-thermal-mechanical model of aluminum-silicon coating, and found that the nugget size and electrode indentation increased with the welding current, so the thermal input increased. However, the width

of the heat-affected zone does not change significantly with the current. In 2019, Zhou and Yao[26] proposed to link the numerical simulation and monitoring means, to obtain a large amount of weld information, and then combined with the numerical simulation methods to establish a set of universal mathematical model suitable for a variety of welding environments. Therefore, this paper studied the resistance spot welding of manganese TRIP steel and DP590 steel as the base material, and studied the connection problem of lightweight materials by using the combination of simulation and experiment.

2. Materials and Methods

The experimental materials are 1.6mm thick medium manganese steel (7MnSteel) and 1.2 mm thick DP590 dual-phase steel. The chemical components of 7MnSteel and DP590 are shown in Table 1 and Table 2, respectively.

The influence of the welding current on the welding performance was studied when the welding time (300 ms) and the electrode pressure (4.5 KN) were unchanged. And also combined with numerical simulation research methods to observe the temperature field, current field, stress field changes in the spot welding process, so as to determine the failure mode of the welded joint.

In this test, the size of all spot welding joint tensile shear test sample is made according to the Global Welding Test Standard Procedure (GWS-5A). The tensile strength and failure mode of the test welding joints, lap joint and sample size are shown in Figure 1.

Table 1. The Chemical Composition Table of 7MnSteel (Wt%).

Mn	C	Si	Cr	Al	N	Pb	P	S	Fe
6.98	0.13	0.22	0.09	0.04	0.0099	0.008	0.006	0.0011	bal.

Table 2. The Chemical Composition Table of DP590 (Wt%)

C	Mn	Si	P	S	Fe
0.071	1.84	0.43	0.011	0.02	bal.
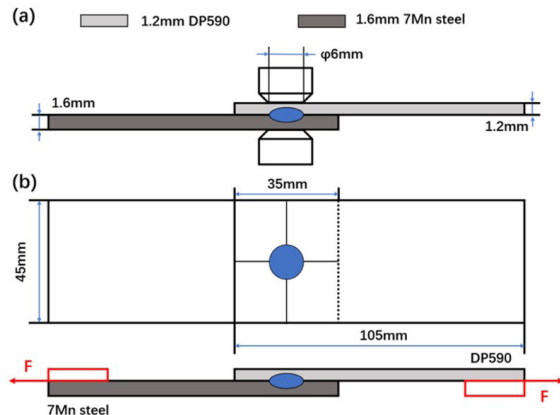
Figure 1. Mechanical test sample: (a) lap joint; (b) tensile sample size.

3. Experimental Results and Analysis

3.1. Influence of welding current on mechanical properties

For tensile test, solder spot failure mode and tensile curve are shown in Figure 2. Unlike the nugget diameter, which increases with increasing spot current in the absence of spatter, the pull shear force of the spot weld joint increases significantly when the welding current is between 7.5kA and 8kA, from 10.35kN to 11.26kN; when the welding current is between 8kA and 9.5kA, the pull shear force of the spot weld joint remains stable. Pouranvari et al.[27] pointed out that although the spatter had no significant effect on the peak load of spot welding, it reduced the ability of energy absorption. Therefore, when the welding current was 9.5kA, the tensile shear force of the spot welded joint did not decrease significantly.

In conclusion, when the welding time is 300 ms and the electrode pressure is 4.5 kN, the optimal welding current should be 9 kA. The nugget diameter is 8.53mm, DP590 side is 14.33%, 7MnSteel side is 15.27%, and the maximum tensile shear is 11.44kN.

3.2. Effects of the welding current on the failure mode

There are four fracture failure modes of tensile shear of resistance spot weldment: interface failure mode (IF), partial interface failure mode (PIF), pull-out failure mode (PF) and partial pull-out failure mode (PF-TT)[28]. When the nugget diameter is small, the interface shear stress reaches the limit shear stress first, and IF failure occurs; when the nugget diameter is greater than the critical diameter, the nugget crack expands faster than the interface shear stress along the plate thickness. The positive tension reaches the limit positive tension first, and the nugget has PF failure[29].

Figure 3 shows the Microstructure analysis and fracture morphology diagram in the IF failure mode, when the welding current is 7.5 kA and the welding time is 300ms under the single pulse conditions. As shown in Figure 3a, for the IF failure
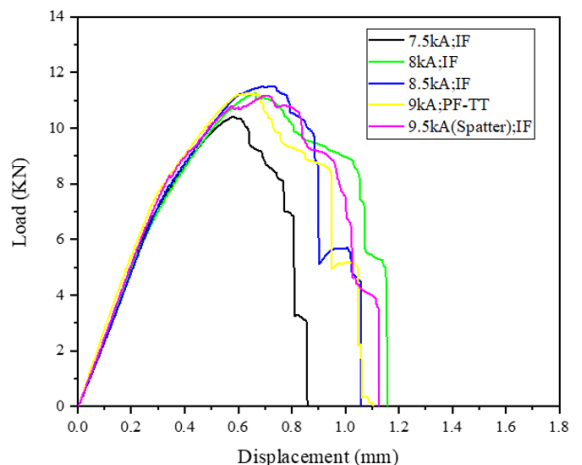
Figure 2. Typical load-displacement curves for different welding currents.

mode, because the welding current is too low, the crack first expands along the center line of the fusion zone (FZ), leading to the separation of the welding plate. The fracture path shown by the white dashed line is almost a straight line parallel to the loading direction. Significant cracks were observed in the heat-affected zone on the 7MnSteel side, about 200 μm to 1000 μm away from the fusion line, and also cracks along the plate thickness in the center of the solder joint, as indicated by yellow arrows. This indicates that IF failure at the solder joint has cracked HAZ initiation on the 7MnSteel side. Figure 3b shows the macroscopic topography diagram of the DP590 side solder joint in IF failure mode. Points c, d and e in Figure 3a and Figure 3b show the fracture positions of the joint in the heat-affected zone, the center line of the nugget and the interior of the nugget, respectively. As shown in Figure 3c, The fracture mode of the joint in the heat-affected zone is brittle fracture, covering the intergranular brittle fracture (red arrow) and the transgranular brittle fracture (orange arrow), which does not show any characteristics of toughness, which indicates that the martensite is brittle in this region, and the secondary crystal boundary cracking can be found in the intergranular region. As shown in Figure 3d, the fracture surface on the center line of the nugget has both brittle and ductile fracture characteristics, which is a mixed fracture of intergranular brittle fracture and transgranular ductile fracture, because the latter consumes more deformation energy than brittle fracture, the binding strength of the joint at this position is higher, so the fracture surface for PF failure mode of toughness fracture generally has better mechanical properties[30]. As shown in Figure 3e, the internal fracture surface of 7MnSteel is a small dimple with a size of less than 5μm, and the fracture mode is a dimple-like ductile fracture, but the area of the fracture surface is very small and has little effect on the binding strength of the whole joint. By comparing the fracture mode of points c, d and e, we can see that in the IF failure mode, the heat-affected zone of the joint is the weakest binding area of the interface, which is actually the center line of the nugget, with the highest binding strength at the internal fracture surface of 7MnSteel.

EDS surface scan analysis was performed at the crack in the heat-affected zone on the side of 7MnSteel in Figure 3a, and the results are shown in Figure 4. According to the scanning results, we can see that there are a large number of C elements and a small amount of Al elements at the crack, and the content of Mn elements is reduced at the fracture position, which is the main reason for the improvement of local hardening and the deterioration of performance and cracking.
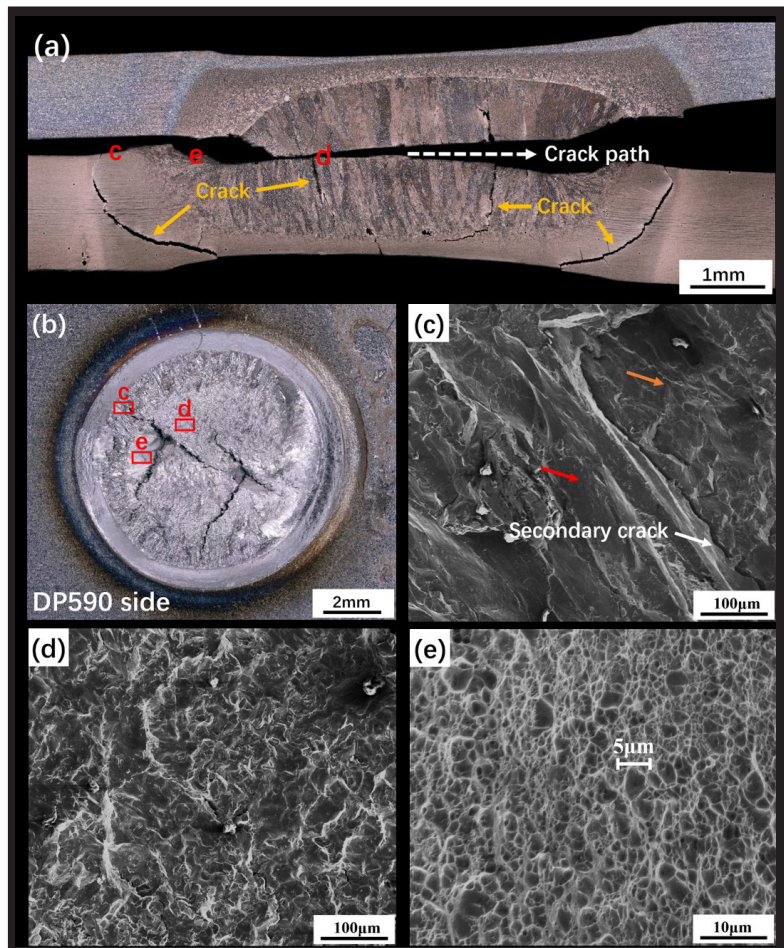
Figure 3. Microstructure analysis and fracture morphology under IF failure mode: (a) Cross-sectional view of solder joints; (b) Macroscopic view of solder joint fracture; (c) c; (d) d; (e) e.

Figure 5 shows the Microstructure analysis and fracture morphology diagram in PF-TT failure mode, and the welding time is 300 ms when the welding current is 9 kA in single-pulse conditions. As shown in Figure 5a, the HAZ on the 7MnSteel side occurs instead of the base material area, and the crack expands into the HAZ on the 7MnSteel plate thickness direction or in the spreading nugget line in the plate thickness direction. The c and d in Figure 5a and Figure 5b are the fracture positions within the joint nugget line and area of 7MnSteel, respectively. As shown in Figure 5c, the fracture mode of the joint at the nugget line is intergranular brittle fracture (red arrow) and piercing brittle fracture (orange arrow), and the grain is rock sugar shaped polygon, which is one of the reasons for the poor mechanical properties of the joint. As shown in Figure 5d and Figure 5e, the internal fracture morphology of 7MnSteel heat-affected zone is toughness fracture, and a large number of small dimples can be observed at the fracture, which indicates that the joint
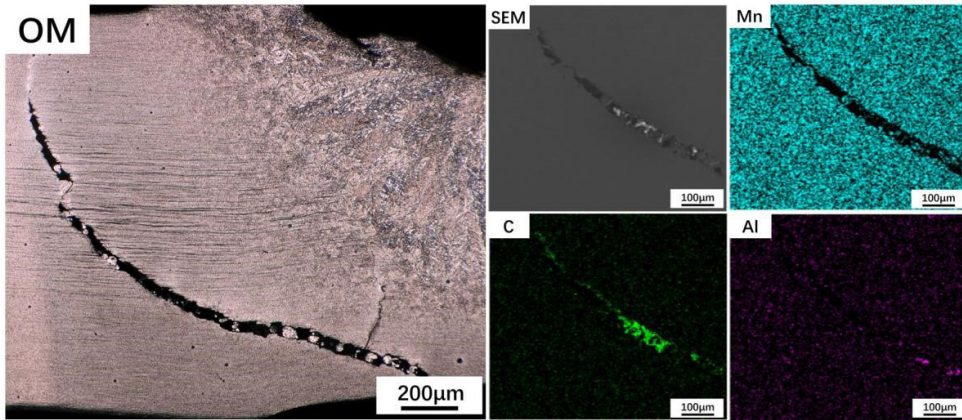
Figure 4. Microstructure diagram and EDS element distribution map at cracks in 7MnSteel.
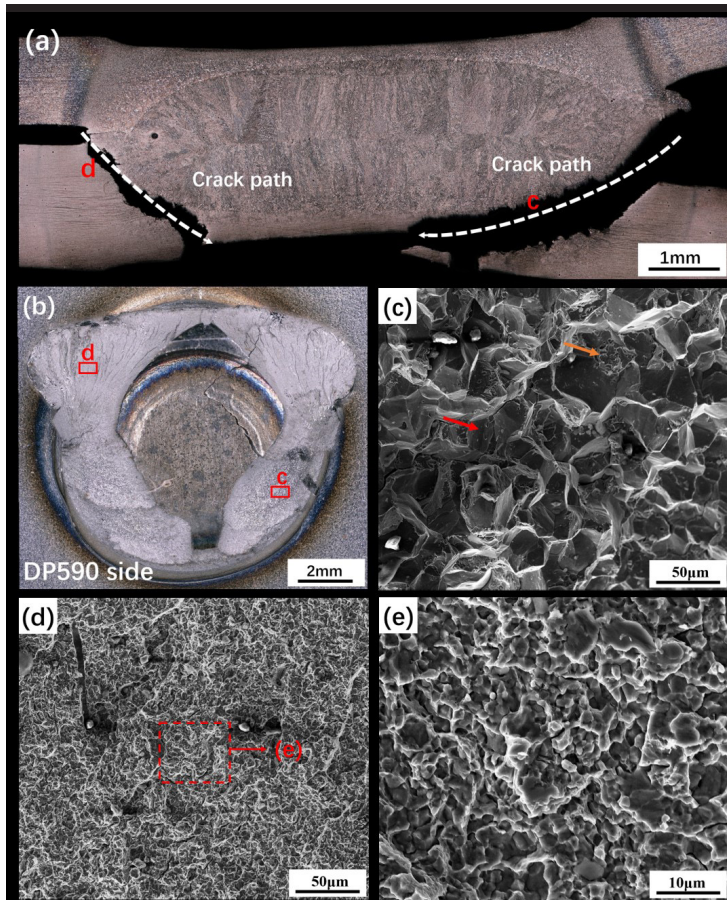
Figure 5. Microstructure analysis and fracture morphology under PF-TT failure mode: (a) Cross-sectional view of solder joints; (b) Macroscopic view of solder joint fracture; (c) c; (d) d; (e) e.

Study on Mechanical Properties and Failure Mechanism of Medium Manganese TRIP Steel / DP590 Dissimilar Steel Resistance Spot Welding Joint

5

has obvious plastic deformation in the process of tensile fracture, and the binding strength of the interface is high.

4. Resistance Spot Welding Numerical Simulation

In this paper, the finite element simulation software ABAQUS is used to establish a coupled thermal-electrical-force model of unequal-thickness 7MnSteel/DP590 dissimilar steel spot welded joints. Both the electrode and the workpiece can be approximated as symmetric, so only 1/4 model (rotated around the axis) is taken for analytical calculations.

4.1. Thermophysical parameters of the material

Using JMatPro software to 7MnSteel and DP590 in the finite element simulation of the thermophysical properties of the parameters used in the solution, the results are shown in Figure 6 and Figure 7, respectively.

4.2. Geometric model and boundary conditions

Figure 8a shows the finite element model of typical resistance spot welding under multi-physical field loading.
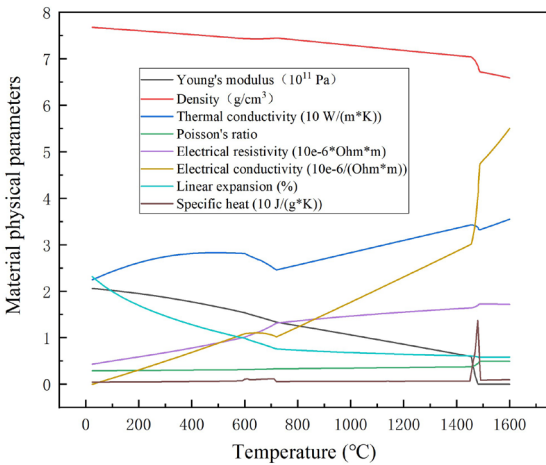
Figure 6. Thermophysical property parameters of 7MnSteel simulated by JMatPro.
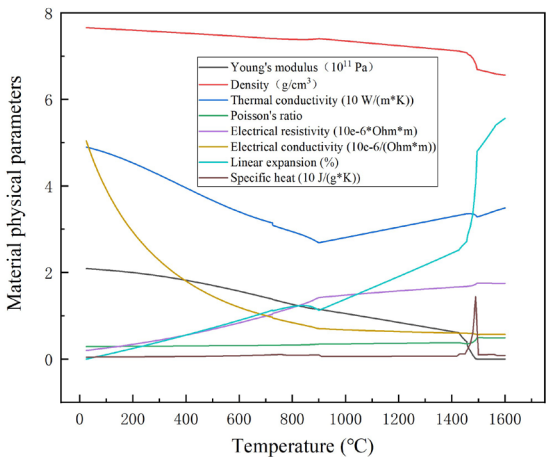
Figure 7. Thermophysical performance parameters of DP590 simulated by JMatPro.

For mechanical boundary conditions, it is necessary to set the symmetry constraint on the symmetry surface, load on the surface of the upper electrode, and the lower electrode is fixed in the simulation, that is, the bottom surface of the lower electrode is set as the full constraint. For the electrical boundary conditions, not only the load current needs to be applied on the end surface of the upper electrode, but also the bottom surface of the lower electrode needs to be set as the surface with potential V=0. For the thermal boundary conditions, the initial temperature of electrode and workpiece is equal to the ambient temperature; the heat dissipation is divided into air heat dissipation on the surface of workpiece and electrode and cooling water heat dissipation inside the electrode, and the air heat dissipation coefficient is set to 0.0194; the cooling water heat dissipation coefficient is set to 3.8.

The grid cells near the three contact areas of electrode-workpiece and workpiece-workpiece are refined. As shown in Figure 8b, the three contact surfaces of the model from top to bottom are the contact surface of the upper electrode and DP590, the contact surface of DP590 and 7MnSteel, and the contact surface of 7MnSteel and the lower electrode. The contact properties include three parts: mechanical contact properties (introduced in the model simplification), thermal contact properties and electrical contact properties. Among them, the thermal contact properties include both interfacial thermal conductivity and interfacial heat generation. The interfacial heat conduction is the heat transfer between the electrode and the workpiece and between the workpiece and the workpiece, and its heat transfer coefficient is related to the temperature. One of the most important parameters is the temperature-dependent interfacial contact conductivity. The temperature-dependent contact properties are shown in Table 3.

4.3. Numerical simulation results analysis

The experimental results show that most of the parameters under the interface failure, in order to study the causes of its failure, the experimental interface failure occurred in the welding parameters selected for stress field, current field and temperature field analysis, the selected parameters are: welding current of 7.5kA, welding time of 300ms, electrode pressure of 4.5kN.
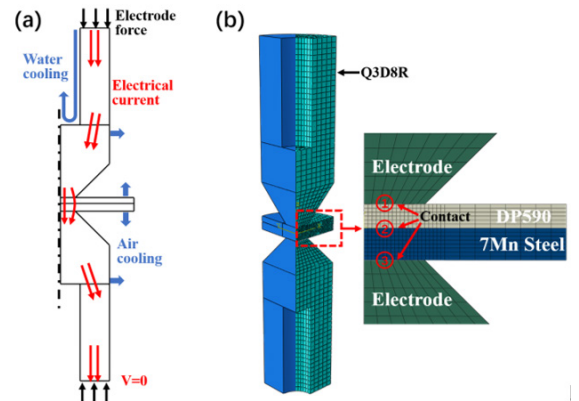
Figure 8. Resistance spot welding model: (a) multi-physics field loading boundary conditions; (b) geometric model and mesh.

Table 3. Contact surface thermoelectric properties and thermal conductivity properties.

Temperature (°C)	Electric conductivity ((Ω·m²)⁻¹×10⁹)		Thermal conductivity (W/(m²·°C)×10⁵)	
	Electrode-workpieces	Workpieces	Electrode-workpieces	Workpieces
21	1.75	0.877	560	140
93	1.8	0.9	620	150
204	1.94	0.927	640	150
315	1.96	0.982	680	150
426	2.16	1.08	720	150
538	2.32	1.16	910	160
650	3.19	2.59	1300	160
760	7.35	3.68	3900	160
870	8.57	4.24	4800	160
982	10	5	5000	160
1093	12.2	6.09	5000	160

4.3.1. Stress field simulation results analysis

Figure 9a for the beginning of the welding phase t = 0.5 ms when the stress distribution trend, the weld plate in the electrode edge location of the stress concentration, which is due to the edge of the end electrode in the electrode pressure and the weld plate extrusion process produces stress concentration, resulting in excessive local pressure. As shown in Figure 9b, when the welding time t = 5 ms, DP590 contact surface and upper electrode at the stress concentration phenomenon was substantially reduced, but 7MnSteel in the lower electrode edge periphery, DP590 and 7MnSteel contact surface in the electrode edge periphery that is 7MnSteel heat affected zone at the stress concentration, stress concentration phenomenon compared to the initial stage of welding more serious, which may also be the reason for the failure of the joint here.

4.3.2. Electric field simulation results analysis

Figure 10a shows the distribution of the current field during resistance spot welding, the denser the weld line is the higher the current density through the area. In Figure 10b for the upper electrode and the upper weld plate contact surface (I-I), the contact surface between the weld plate (II-II) and the lower electrode and the lower weld plate contact surface (Ⅲ-Ⅲ), (I-I) and (Ⅲ-Ⅲ) contact surface current density distribution is similar, reaching a maximum at the edge of the electrode, then gradually decreasing from both ends to the center and then stabilizing; II-II contact surface current density in the middle of the constant, the distribution of the current field in the spot welding process is shown in Figure 10c, and the trend of current density distribution is the same as the theoretical current density distribution in Figure 10a and Figure 10b, which verifies the reliability of the numerical simulation.

4.3.3. Temperature field simulation results analysis

As shown in Figure 11a, the temperature of the electrode and workpiece contact surface and workpiece and workpiece contact surface are the first to rise during the energized welding stage t = 0.5 ms. Due to the edge effect of the current, the current is concentrated in the electrode edge area of the electrode-welding plate contact surface, the current density is higher, the temperature of the electrode edge area relative to the temperature rise in the central area is more pronounced. As shown in Figure 11b, in the energized welding stage t = 5 ms, the contact resistance with the welding process and rapidly decreasing, the workpiece internal resistance generated by resistance heat began to dominate, coupled with the cooling water in the copper electrode water cooling heat dissipation effect, the center of the nugget rapidly warming, it can be seen that the radial nugget size growth rate is significantly higher than the axial, which is due to the water cooling effect, the welding process in the axial direction heat dissipation coefficient is much greater than the radial, in addition to the radial length of the range of contact resistance, so the radial direction of the molten nucleus resistance heat is more concentrated, the nugget growth rate is faster. As shown in Figure 11c, the nugget size grows rapidly during the energized welding stage t = 100ms. It can also be seen that the 7MnSteel side of the weld plate of the nucleus growth rate is significantly greater than the DP590 side of the production rise, this is due to 7MnSteel has a higher resistivity and lower thermal conductivity compared to DP590, more heat production per unit of time, the faster the nugget growth rate. As shown in Figure 11d, in the power welding stage t = 300 ms, the edge of the nugget region produced a smaller deformation, the growth rate of the nugget size compared to the previous also slowed down significantly, DP590 side of the nugget diameter and 7MnSteel side of the nugget diameter size is the same, this is due to the overall temperature of the welded joint are in a higher state, the contact resistance with the temperature rise and dramatic decrease. In addition, the actual workpiece-workpiece contact area gradually becomes larger due to the continuous growth of the nugget, and the current density decreases. The combined effect of the two factors leads to a significant decrease in the growth rate of the nugget.

5. Numerical Simulation and Comparison of Experimental Results

In the single pulse process, set the welding time of 300ms, electrode pressure of 4.5 kN, pre-pressure time of 300 ms, holding time of 40ms, varying the welding machine current, comparative study of 7MnSteel/DP590 dissimilar

Study on Mechanical Properties and Failure Mechanism of Medium Manganese TRIP Steel / DP590 Dissimilar Steel Resistance Spot Welding Joint

7
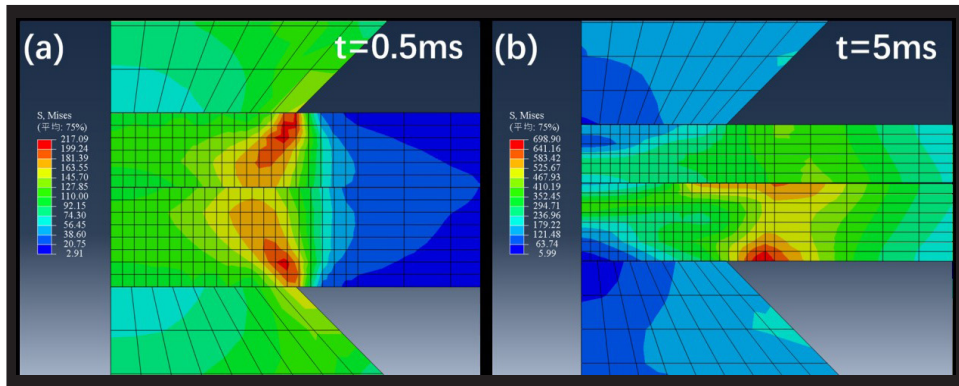
Figure 9. Stress field analysis during welding: (a) t=0.5ms; (b) t=5ms.
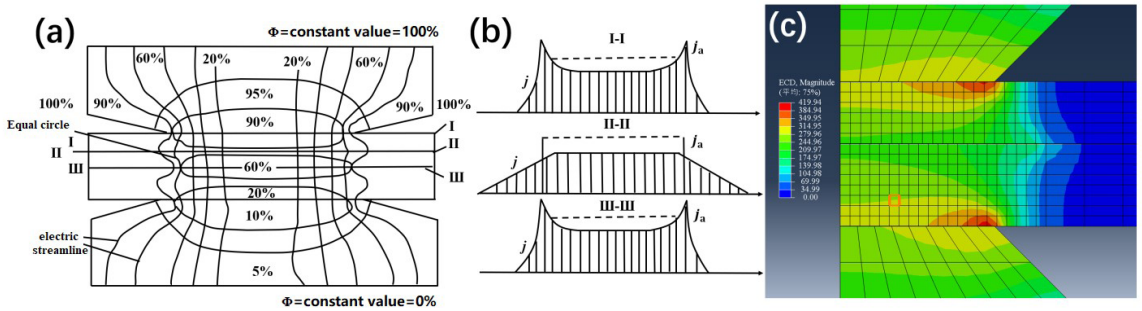
Figure 10. Current field analysis during welding: (a) current field distribution; (b) current density distribution; (c) ABAQUS simulation current density distribution.
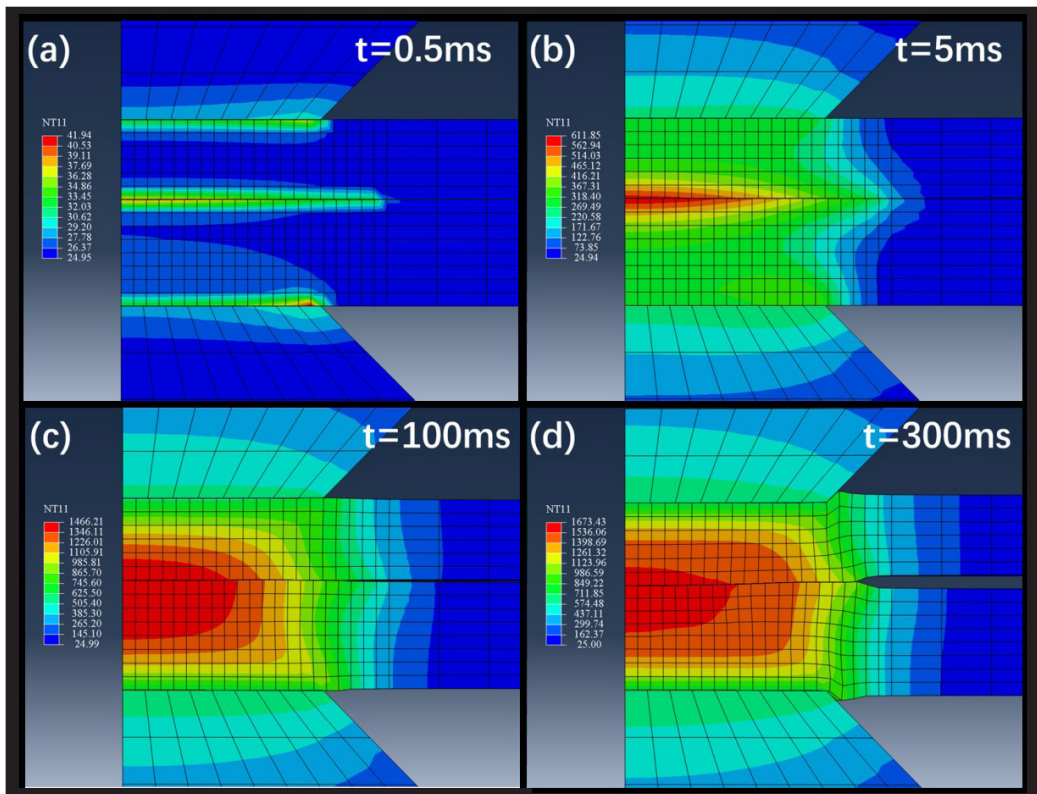
Figure 11. Temperature field analysis during welding: (a) t=0.5ms; (b) t=5ms; (c) t=100ms; (d) t=300ms.

Table 4. Spot welding joint simulation and experimental nugget diameter comparison.

Welding current (kA)	Simulated nugget diameter (mm)	Experimental nugget diameter (mm)	Error(%)
7.5	7.33	6.86	6.85
8	7.56	7.17	5.43
8.5	8.31	7.98	4.13
9	8.64	8.53	1.29
9.5 (spatter)	8.83	6.63	33.18

steel resistance spot welding process test and numerical simulation of the nugget diameter, the results are shown in Table 4. As the simulation does not take into account the spatter of the welded joint, when the spatter of the welded joint, the experimentally measured nugget diameter rapidly decreases, the simulation appears to be a large error. In the welding numerical simulation and experimental measurement of the nugget diameter error within 7%, verifying the accuracy and reliability of the resistance spot welding finite element model.

5. Conclusion

This paper studies the influence of welding current parameters on the mass and mechanical properties of 7MnSteel/DP590 points, and analyzes the failure mode of the joint. In addition, the spot welding process is numerically simulated. The final conclusion is as follows:

(1) The optimal welding current parameter was determined to be 9kA under a single pulse by the control variable method. The diameter of the weld nugget under the optimal single pulse process is 8.53 mm, DP590 side is 14.33%, 7MnSteel side is 15.27%, and the maximum tensile shear is 11.44 kN.

(2) The welding joint failure mode under single pulse process is PF-TT failure; welding current is 8.5 kA, welding time is 400 ms, PIF failure when electrode pressure is 4.5 kN is used, and the other samples are IF failure. When IF fails, the heat-affected zone, the center line on the nugget and the internal fracture of the nugget are brittle fracture, mixed fracture and toughness fracture, respectively. In this failure mode, cracks have already appeared in the heat-affected zone of the 7MnSteel side, with the segregation of C elements and Al elements; the other is PF-TT failure, the nugget of the 7MnSteel side is stripped out, and the internal fracture at the nugget line and the 7MnSteel heat-affected zone are brittle fracture and toughness fracture respectively.

(3) Through simulation, it is found that the stress concentration of the welding plate at the edge of the electrode at the beginning stage of welding occurs, and the stress concentration appears in the 7MnSteel heat-affected zone, which may also be the reason for the failure of the joint here. The current density is concentrated at the electrode and the welding plate contact surface, and the simulated and experimental

nugget error is within 7%, verifying the accuracy and reliability of the model.

7. References

1. Ozsarac U. Investigation of mechanical properties of galvanized automotive sheets joined by resistance spot welding. J Mater Eng Perform. 2012;21(5):748-55.
2. Shi J, Hu J, Wang C, Wang CY, Dong H, Cao WQ. Ultrafine grained duplex structure developed by ART-annealing in cold rolled medium-Mn steels. J Iron Steel Res Int. 2014;21(2):208-14.
3. Grajcar A, Kuziak R, Zalecki W. Third generation of AHSS with increased fraction of retained austenite for the automotive industry. Arch Civ Mech Eng. 2012;12(3):334-41.
4. Aydin H, Essadiqi E, Jung IH, Yue S. Development of 3rd generation AHSS with medium Mn content alloying compositions. Mater Sci Eng A. 2013;564:501-8.
5. Wang MM, Tasan CC, Ponge D, Raabe D. Spectral TRIP enables ductile 1.1 GPa martensite. Acta Mater. 2016;111:262-72.
6. Suh DW, Kim SJ. Medium Mn transformation-induced plasticity steels: recent progress and challenges. Scr Mater. 2017;126:63-7.
7. Han J, Silva AK, Ponge D, Raabe D, Lee S-M, Lee Y-K, et al. The effects of prior austenite grain boundaries and microstructural morphology on the impact toughness of intercritically annealed medium Mn steel. Acta Mater. 2017;122:199-206.
8. Han J, Lee SJ, Jung JG, Lee YK. The effects of the initial martensite microstructure on the microstructure and tensile properties of intercritically annealed Fe–9Mn–0.05 C steel. Acta Mater. 2014;78:369-77.
9. Brauser S, Pepke LA, Weber G, Rethmeier M. Deformation behaviour of spot-welded high strength steels for automotive applications. Mater Sci Eng A. 2010;527(26):7099-108.
10. Messler JRW Jr, Jou M. Review of control systems for resistance spot welding: past and current practices and emerging trends. Sci Technol Weld Join. 2014;1(1):1-9.
11. Martín Ó, Tiedra PD, San-Juan M. Combined effect of resistance spot welding and precipitation hardening on tensile shear load bearing capacity of A286 superalloy. Mater Sci Eng A. 2017;688:309-14.
12. Akkaş N. Welding time effect on tensile-shear loading in resistance spot welding of SPA-H weathering steel sheets used in railway vehicles. Acta Phys Pol A. 2017;131(1):52-4.
13. Jia Q, Liu L, Guo W, Peng Y, Zou G, Tian Z, et al. Microstructure and tensile-shear properties of resistance spot-welded medium Mn steel. Metals. 2018;8(1):48.
14. Park G, Kim K, Uhm S, Lee C. A comparison of cross-tension properties and fracture behavior between similar and dissimilar resistance spot-weldments in medium-Mn TRIP steel. Mater Sci Eng A. 2019;752:206-16.
15. Li S, Yang S, Lu Q, Luo H, Tao W. A novel shim-assisted resistance spot welding process to improve weldability of medium-Mn transformation-induced plasticity steel. Metall Mater Trans, B. 2019;50:1-9.
16. Zhao D, Wang Y, Zhang P, Liang D. Modeling and experimental research on resistance spot welded joints for dual-phase steel. Materials. 2019;12(7):1108.
17. Hamidinejad SM, Kolahan F, Kokabi AH. The modeling and process analysis of resistance spot welding on galvanized

Study on Mechanical Properties and Failure Mechanism of Medium Manganese TRIP Steel / DP590 Dissimilar Steel Resistance Spot Welding Joint

9

steel sheets used in car body manufacturing. Mater Des. 2012;34:759-67.

18. Lee Y, Jeong H, Park K, Kim Y, Cho J. Development of numerical analysis model for resistance spot welding of automotive steel. J Mech Sci Technol. 2017;31(7):3455-64.

19. Nied HA. The finite element modeling of the resistance spot welding process. Weld J. 1984;63(4):123-32.

20. Tsai CL, Dai WL, Dickinson DW, Papritan JC. Analysis and development of a real time control methodology in resistance spot welding. Weld J. 1991;70(20):339-51.

21. Tsai CL, Jammal OA, Papritan JC, Dickinson DW. Modeling of resistance spot weld nugget growth. Weld J. 1992;71(2):47-54.

22. Browne DJ, Chandler HW, Evans JT, Wen J. Computer simulation of resistance spot welding in aluminum: part I. Weld J. 1995;74(10):339-44.

23. Murakawa H, Kimura H, Ueda Y. Weldability analysis of spot welding on aluminum using FEM. Trans JWRI. 1995;24(2):101-11.

24. Raoelison RN, Fuentes A, Pouvreau C, Rogeon P, Carré P, Dechalotte F. Modeling and numerical simulation of the resistance spot welding of zinc coated steel sheets using rounded tip electrode: analysis of required conditions. Appl Math Model. 2014;38(9-10):2505-21.

25. Lu Y, Peer A, Abke T, Kimchi M, Zhang W. Subcritical heat affected zone softening in hot-stamped boron steel during resistance spot welding. Mater Des. 2018;155:170-84.

26. Zhou K, Yao P. Overview of recent advances of process analysis and quality control in resistance spot welding. Mech Syst Signal Process. 2019;124:170-98.

27. Pouranvari M, Abedi A, Marashi P, Goodarzi M. Effect of expulsion on peak load and energy absorption of low carbon steel resistance spot welds. Sci Technol Weld Join. 2013;13(1):39-43.

28. Pouranvari M, Marashi SPH. Critical review of automotive steels spot welding: process, structure and properties. Sci Technol Weld Join. 2013;18(5):361-403.

29. Pouranvari M, Asgari HR, Mosavizadch SM, Marashi PH, Goodarzi M. Effect of weld nugget size on over load failure mode of resistance spot welds. Sci Technol Weld Join. 2007;12(3):217-25.

30. Li S, Yang S, Lu Q, Luo H, Tao W. A novel shim-assisted resistance spot welding process to improve weldability of medium-mn transformation-induced plasticity steel. Metall Mater Trans, B, Process Metall Mater Proc Sci. 2019;50(1):1-9.